



# CHORUS

This is the accepted manuscript made available via CHORUS. The article has been published as:

## Calibrated simulations of Z opacity experiments that reproduce the experimentally measured plasma conditions

T. Nagayama, J. E. Bailey, G. Loisel, G. A. Rochau, J. J. MacFarlane, and I. Golovkin

Phys. Rev. E **93**, 023202 — Published 5 February 2016

DOI: [10.1103/PhysRevE.93.023202](https://doi.org/10.1103/PhysRevE.93.023202)

# Calibrated simulations of Z opacity experiments that reproduce the experimentally measured plasma conditions

T. Nagayama, J. E. Bailey, G. Loisel, and G. A. Rochau  
*Sandia National Laboratories, Albuquerque, New Mexico 87185, USA*

J. J. MacFarlane and I. Golovkin  
*Prism Computational Sciences, Madison, Wisconsin 53703, USA*

Recently, frequency-resolved iron opacity measurements at electron temperatures of 170 – 200 eV and electron densities of  $0.7 - 4.0 \times 10^{22} \text{ cm}^{-3}$  revealed a 30 – 400% disagreement with the calculated opacities [J. E. Bailey *et al.*, *Nature* **517**, 56 (2015)]. The discrepancies have a high impact on astrophysics, atomic physics, and high energy density physics, and it is important to verify our understanding of the experimental platform with simulations. Reliable simulations are challenging because the temporal and spatial evolution of the source radiation and of the sample plasma are both complex and incompletely diagnosed. In this article we describe simulations that reproduce the measured temperature and density in recent iron opacity experiments performed at the Sandia National Laboratories Z facility. The time-dependent spectral irradiance at the sample is estimated using the measured time- and space-dependent source radiation distribution, in-situ source-to-sample distance measurements, and a 3-D view-factor code. The inferred spectral irradiance is used to drive 1-D sample radiation hydrodynamics simulations. The images recorded by slit-imaged space-resolved spectrometers are modeled by solving radiation transport of the source radiation through the sample. We find that the same drive radiation time history successfully reproduces the measured plasma conditions for eight different opacity experiments. These results provide a quantitative physical explanation for the observed dependence of both temperature and density on the sample configuration. Simulated spectral images for the experiments without the FeMg sample shows quantitative agreement with the measured spectral images. The agreement in spectral profile, spatial profile, and brightness provides further confidence in our understanding of the backlight-radiation time history and image formation. These simulations bridge the static-uniform picture of the data interpretation and the dynamic-gradient reality of the experiments and will allow us to quantitatively assess the impact of effects neglected in the data interpretation.

## I. INTRODUCTION

Opacity quantifies photon absorption in matter and plays a crucial role in many high energy density (HED) plasmas, including inertial confinement fusion plasmas and stellar interiors [1–3]. Modeling opacity is especially challenging for partially ionized plasmas at HED conditions because it requires approximations that have limited to no experimental validation. The lack of benchmark experiments leads to the inability to verify the theoretical constructs used to calculate/simulate opacity in HED plasmas. This causes uncertainty in understanding plasma evolution. For example, solar evolution models do not accurately predict the location of the boundary between the solar convection zone and the radiative zone [4]. One hypothesis is an underestimate in the calculated opacities used in the solar models [4]; a 15% increase in the calculated solar mean opacity would resolve this problem [5]. At the solar convection zone base (CZB), the main opacity contributors are O, Ne, and Fe. Since the opacity calculation complexity increases with the number of bound electrons, one likely source of discrepancy is inaccuracy of the calculated Fe opacity [6].

In 2007, Fe opacities were successfully measured at  $T_e=156$  eV and  $n_e = 6.9 \times 10^{21} \text{ cm}^{-3}$  at the Sandia National Laboratories (SNL) Z machine[7]. While both  $T_e$  and  $n_e$  were significantly lower than those at CZB,

Fe opacities with similar charge state distribution as at the CZB were measured for the first time. More recently, the experiments were improved to increase both  $T_e$  and  $n_e$  [8], and Fe opacities were measured at various conditions relevant to stellar interiors (i.e., electron temperatures,  $T_e = 170 - 200$  eV, and electron density,  $n_e = 0.7 - 4.0 \times 10^{22} \text{ cm}^{-3}$ ) [9]. These measurements revealed a 30 – 400% disagreement between the measured and modeled frequency-dependent Fe opacities as  $T_e$  and  $n_e$  approach the CZB conditions. The solar mean opacity at the CZB was recomputed with the measured Fe opacity, and it increased by 7%. This is roughly half of the mean-opacity correction needed to resolve the solar CZB problem. Such severe discrepancies have significant impacts on astrophysics, atomic physics, and HED physics, and therefore it is critical to ensure that the discrepancies were not caused by experimental flaws.

Experimental opacity platforms have been developed over the last few decades [10–20]. The sample transmission,  $T_\nu$ , and opacity,  $\kappa_\nu$  [ $\text{cm}^2/\text{g}$ ], are related to the incident backlight radiation,  $I_0$ , and the radiation attenuated by the sample,  $I_\nu$ , by:

$$T_\nu = \frac{I_\nu}{I_0} = e^{-\kappa_\nu \rho L} \quad (1)$$

where  $\nu$  is the photon frequency,  $\rho$  is the sample mass density in  $\text{g}/\text{cm}^3$ , and  $L$  is the sample thickness in cm.

The details of the atomic and plasma physics that control the opacity are revealed in the spectral features of  $T_\nu$ . Therefore, measuring the frequency-resolved sample transmission helps to investigate the accuracy of the opacity models.

At SNL, a cylindrically imploding plasma called a z-pinch dynamic hohlraum (ZPDH) [21] provides powerful radiation that volumetrically heats a target. This target consists of a thin-foil FeMg *sample* sandwiched by Be and/or CH, which we call a *tamper*. The implosion stagnates on the  $z$  axis, provides bright backlight radiation, and permits measurements of sample-attenuated and -unattenuated spectra on x-ray films (see Sec. II for more details). Fe transmission can be inferred from the measured spectra using Eq. (1). The Fe temperature and density are inferred from the measured Mg K-shell lines [8]. Fe opacities are calculated at the inferred conditions and compared against the measured opacities to benchmark the calculation [9].

One concern is the accuracy of the data interpretation. Currently, the data are interpreted as if the plasma conditions were constant and uniform. While the backlight duration provides an effectively time resolved measurement, the sample plasma conditions are not completely uniform, changing gradually over the few-ns backlight duration. Thus, it is important to understand the plasma evolution over the backlight duration.

The goal of this article is to perform calibrated 1-D hydrodynamic simulations of the opacity experiments, to better bridge the static-uniform picture used in the data interpretation with the dynamic-gradient reality in the experiments. We do not attempt to perform an ab-initio simulation that would require 3-D descriptions of both the ZPDH and the sample/tamper plasma evolution. Even simulating the ZPDH itself is complex enough to challenge state of the art capabilities [22] and the interaction of the ZPDH plasma and radiation with the sample adds even more difficulties. Furthermore, if the Fe opacity is inaccurate, such detailed simulation would provide inaccurate FeMg sample plasma evolution. For example, if the calculated Fe opacity is indeed lower than actual opacity as reported in Ref. [9], such ab-initio simulation would predict lower temperature because radiation energy absorbed by the plasma is underestimated. Therefore, to avoid this dilemma, we need to somehow insulate the hydrodynamic simulations from the uncertainties in the Fe opacity. This can be achieved by calibrating the simulations so that they reproduce the  $T_e$  and  $n_e$  inferred with Mg K-shell spectroscopy. Such calibrated simulations provide better insight into the experiments and will help to numerically quantify the impact of various potential sources of errors such as plasma self-emission, tamper-attenuation, time-and-space integration, and non-local thermodynamic equilibrium effects.

In this article, we simulate the target (i.e., FeMg sample and Be/CH tamper) plasma hydrodynamics and the image formation on the detector guided by various mea-

surements. First, the time-dependent spectral irradiance at the FeMg sample is estimated using a 3-D view-factor code with the measured pre-refurbished ZPDH 2-D radiation time history and the in-situ, measured source-to-sample distances as its input (see Sec. III A). The 1-D target plasma hydrodynamics is, then, simulated using the inferred spectral irradiance. Finally, the image formation on the detector is simulated by solving radiation transport of the ZPDH radiation through the simulated target plasma evolution accounting for the effects of the aperture and slits. To calibrate the simulation, the measured source radiation needs to be scaled up by a factor of 2.6 to account for an increased ZPDH radiation output after the Z refurbishment [23] in 2007 and potentially to account for Fe-opacity inaccuracy. With this calibration factor,  $T_e$  and  $n_e$  inferred from simulated spectra agreed with measured ones for eight different experiments. This calibration factor also allows the simulated backlighter spectral image to agree with the measured spectral image both in spectral/spatial shape and in brightness. These quantitative agreements support the soundness of the simulations.

The simulations refine the understanding of our opacity experiments. We find <10% sample axial gradients in  $T_e$  and  $n_e$  at each temporal point, and  $T_e$  and  $n_e$  decrease by 14% and 70%, respectively, over the backlight duration. While those temporal gradients do not sound negligible, their impact on our opacity measurements were found to be small [9]. The detailed radiation modeling clarifies the relationship between the time history of the sample heating and evolution and the backlight time history.

The new simulations provide a physical explanation of why the sample temperature depends on the target configuration. This was not explained by the previous simulations [24]. The simulations reported here show that the higher temperature arises because the sample-to-source distance is anti-correlated with the top-tamper mass. The sample with lighter top-tamper are hydrodynamically pushed farther away from the radiation source due to the pressure supplied from the bottom by the ZPDH plasma and the expansion of the bottom-tamper. The larger distance causes more geometric dilution of the source radiation, and the sample is consequently heated less (Sec. V B). Refining our understanding of the sample heating will promote better control over sample conditions in future experiments and also help us to quantify the impact of the complex sample evolution on our opacity measurements.

The discussion of these findings is organized as follows. Sec. II describes the Z opacity experiments and summarizes how Fe conditions and opacity are determined. Sec. III describes three phases of our simulations: modeling heating radiation (Sec. III A), simulating sample hydrodynamics (Sec. III B), and modeling image formation on the detector while accounting for instrumental geometry effects and radiation transport through the sample (Sec. III C). Limitations of the simulations are discussed in

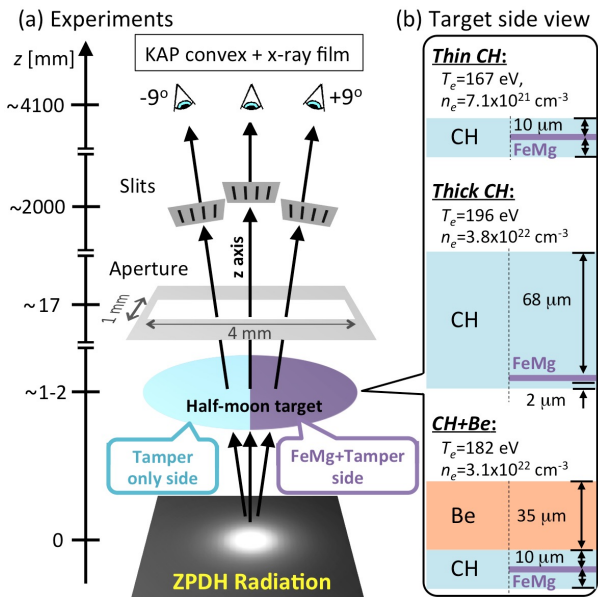


FIG. 1. (Color online) (a) The experimental configuration employs a half-moon target and spectrometers fielded at  $0^\circ$  and  $\pm 9^\circ$  with respect to the  $z$  axis. This experimental geometry dictates the backlight radiation projected through different parts of the target and allows measurements of the FeMg-plus-tamper-attenuated and tamper-only-attenuated spectra in a single experiment. (b) Cross-sections of the various half-moon target configurations, their labels, and the typical conditions. The tamper mass above the sample controls the sample conditions. Images are not to scale.

Sec. IV. We conclude by summarizing the refinement of our understanding, provided by the simulations, of the backlight radiation and sample heating.

## II. Z OPACITY SCIENCE PLATFORM

The SNL Z opacity experimental setup is shown in FIG. 1. The *half-moon* target consists of a thin semi-circular FeMg sample sandwiched by circular tampers. Three tamper configurations are *Thin CH* (i.e., 20- $\mu$ m CH), *Thick CH* (i.e., 70- $\mu$ m CH), and *CH+Be* (i.e., 20- $\mu$ m CH plus 35- $\mu$ m Be), as shown in FIG. 1 (b).

The half-moon target is placed above the ZPDH radiation source [6, 21] and radiatively heated as the ZPDH plasma implodes. In FIG. 2, gated broadband pinhole images of the ZPDH radiation measured without the aperture show how a cylindrical radiative shock propagates and stagnates at the central axis. The radiation intensity spatial distribution changes with time, and this information is critical to accurately understand the sample plasma hydrodynamics (Sec. III A and III B) and the spectral image formation on the detector (Sec. III C).

The ZPDH radiation supplies the heating radiation from the sample's point of view and the backlight radiation from the detector's point of view. The sample

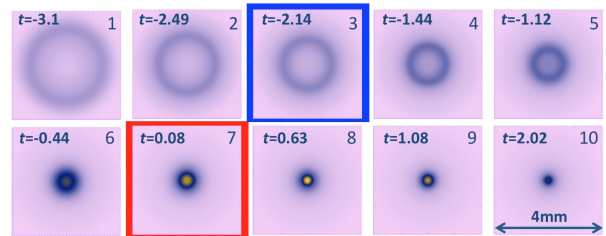


FIG. 2. (Color online) Gated pinhole images of the pre-rufurnished ZPDH radiation measured for an experiment without the aperture. The images are azimuthally smoothed. The gate time,  $t$ , is indicated in ns with respect to the backlight radiation peak and the frame numbers are shown in the upper right corner of each image.

is close to the radiation source and is heated by the radiation emitted from the entire ZPDH (Sec. III A). At stagnation, the ZPDH radiation transmitted through the sample is measured by potassium acid phthalate (KAP) crystal spectrometers, which are fielded along  $\pm 9^\circ$  with respect to the  $z$  axis as shown in FIG. 1 [25, 26]. On-axis data are available for some experiments as well. Due to the aperture and the spectrometer slits, the radiation observed by the detector peaks around the time of the ZPDH stagnation (Sec. III C, Appendices A and B).

Slits provide spatial resolution across the half-moon boundary. Since the ZPDH radiation source is some distance away from the half-moon target, it backlights different locations of the sample, i.e., FeMg-embedded side for the spectrometer at  $+9^\circ$  and tamper-only side for the spectrometer at  $-9^\circ$ . This permits the measurement of the sample-attenuated (at  $+9^\circ$ ) and -unattenuated (at  $-9^\circ$ ) spectra in a single experiment as shown in FIG. 3. The data are recorded on x-ray film.

The Fe conditions are inferred by analyzing Mg K-shell lines appearing at  $\lambda < 9.5$   $\text{\AA}$  [8, 26]. *Thin CH*, *Thick CH*, and *CH+Be* configurations achieved different Fe conditions as shown in Fig. 1(b) [8, 9]. For each tamper configuration, multiple experiments were performed with different Fe thicknesses. We confirmed that varying the Fe thickness did not alter the Fe conditions, which supports the volumetric heating assumption. Finally, the FeMg transmission spectra at those conditions are extracted by dividing  $I_V^{+9^\circ}$  by  $I_V^{-9^\circ}$ . This *static-uniform-plasma* picture used to interpret our measurements needs to be verified by the *dynamic-gradient-plasma* picture with the simulation developed here.

## III. SIMULATING Z FE-OPACITY MEASUREMENTS

### A. Modeling heating radiation on the sample

To simulate the sample/tamper plasma evolution, one must know the drive-radiation time history. As shown in FIG. 1, the sample is heated by the ZPDH radiation

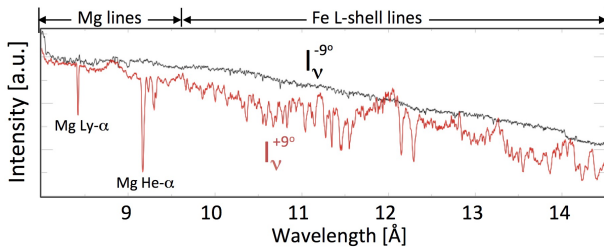


FIG. 3. (Color online) Measured FeMg-attenuated,  $I_V^{+9^\circ}$ , and -unattenuated,  $I_V^{-9^\circ}$ , spectra from a single experiment. Mg lines are analyzed to characterize the sample  $T_e$  and  $n_e$ , and FeMg transmission at those conditions can be inferred by  $T_V^{FeMg} \approx I_V^{+9^\circ} / I_V^{-9^\circ}$ .

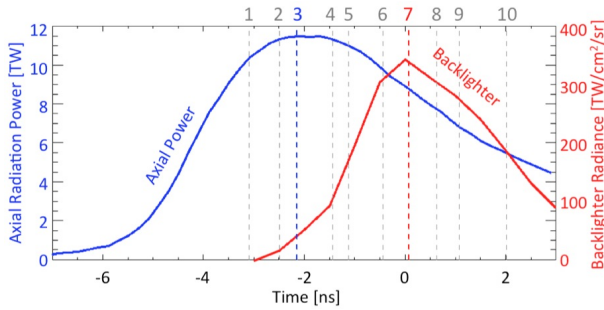


FIG. 4. (Color online) The blue and the red curves are the radiation power time history measured on the pre-refurbished Z facility with x-ray diodes and the backlight-radiance time history simulated in Sec. VC, respectively. Dashed lines indicate the timing of each pinhole image. The blue and the red dashed lines correspond to the frames closest to the axial-power peak and to the backlight-radiance peak, respectively.

source below the sample. Modeling the heating radiation at the opacity sample is complex because, at each time, one has to take into account the ZPDH radiation intensity spatial distribution and the 3-D view factors between the sample and the radiation source.

A comprehensive set of radiation source characterization measurements was compiled on the pre-refurbishment Z facility. FIG. 2 shows the gated broadband x-ray ( $> 800$  eV) pinhole images of the ZPDH radiation source measured without the aperture. These images are azimuthally averaged for modeling purposes, and their intensities are calibrated with the axial radiation power measured with x-ray diodes (XRD), which is shown as the blue curve in FIG. 4. The red curve in FIG. 4 is the backlight time history discussed in detail in Sec. VA.

Unfortunately, the pinhole images and the XRD measurements are available only for the ZPDH before the Z refurbishment in 2007. After the refurbishment, the electrical energy delivered to the load was roughly doubled, and the output radiation was significantly increased [21]. We are currently measuring the axial power time history and the calibrated ZPDH radiation pinhole images. Preliminary data show that the radiative shock velocity of

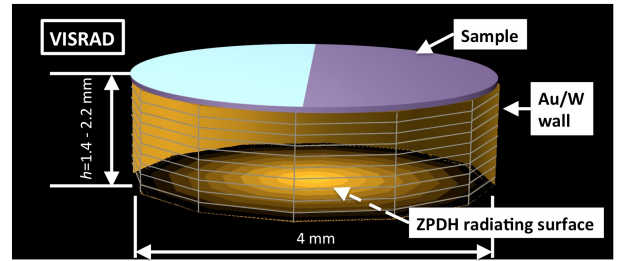


FIG. 5. (Color online) VISRAD defines emitting components (i.e., ZPDH) and the sample location in a 3-D space. VISRAD solves the 3-D view factors between the sample and each emitting component and computes the heating radiation time history on the sample.

the new ZPDH is the same as that of the old one within the measurement uncertainties. Also, the emergent intensity on the film is roughly doubled over  $6 - 14$  Å [21]. In this article, the heating radiation is computed with the old-ZPDH intensity images scaled by a factor of 2.6 (FIG. 4). This scaling constant was calibrated so that the resultant heating radiation drives the sample to reach the measured temperatures (Sec. III B).

The heating radiation time history on the sample is modeled with the 3-D view-factor code VISRAD [27] using information constrained by measurements. First, we define the geometry of the radiation source, sample, and surrounding components in VISRAD as shown in FIG. 5. The ZPDH radiation source is approximated as a collection of multiple concentric rings. The radiation power time history of each ring is extracted from the scaled pinhole images (FIG. 2) and assigned to each ZPDH component in VISRAD. Recently, we found that the sample temperature was anti-correlated with the measured source-to-sample distance [28]. Experiments with the same tamper configurations achieved similar source-to-sample distances and similar sample temperatures. Thus, the source-to-sample distances,  $h$ , representative for each tamper configuration are estimated by averaging the measurements over the same tamper configurations. They are 2.2 mm for *Thin CH*, 1.5 mm for *CH+Be*, and 1.4 mm for *Thick CH* [28].

The boundary surrounding the space between the sample and the ZPDH radiating surface is approximated by a 100% reflective Au/W wall. This assumption is reasonable because the surrounding Au hardware and ZPDH tungsten plasma prevent radiation from escaping and because a large fraction of the source radiation is re-emitted by the Au and W. In FIG. 5, the front side of the Au/W wall is made transparent for display purposes so that the ZPDH radiating surface can be displayed.

Once the geometry and radiation source are defined, VISRAD takes into account the 3-D view factors between the sample, ZPDH radiation source, and the re-emitting components and computes the heating radiation time history experienced by the sample. The limitations are discussed in Sec. IV.

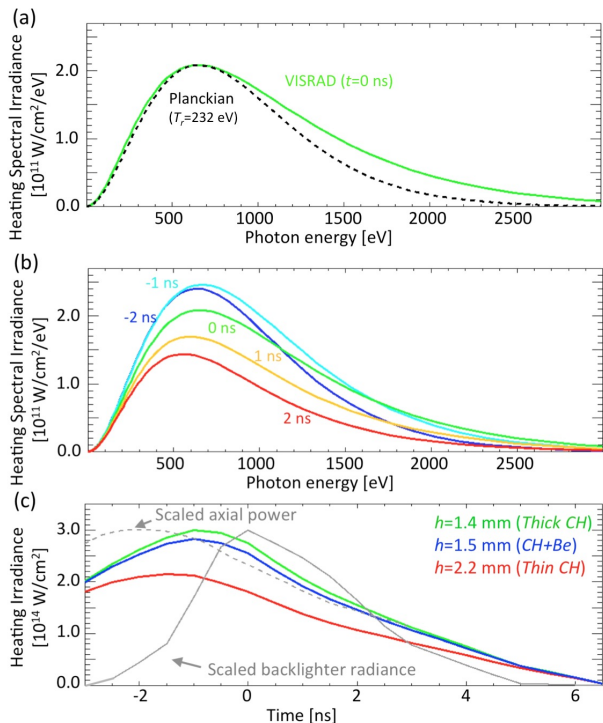


FIG. 6. (Color online) (a) Comparison of a simulated heating spectral irradiance at  $t = 0$  ns with a scaled Planckian distribution. (b) Simulated heating spectral irradiance at  $t = -2, -1, 0, +1,$  and  $+2$  ns for the *Thick CH* sample (i.e.,  $h = 1.4$  mm). (c) Heating radiance time histories computed at  $h = 1.4, 1.5,$  and  $2.2$  mm. Gray solid and dashed lines are the scaled backlighter radiance and the scaled axial power, respectively.

FIG. 6(a) compares simulated VISRAD heating radiation at  $t = 0$  ns with a scaled 232-eV Planckian distribution. 232 eV is selected to reproduce the intensity peak of the VISRAD heating radiation. The comparison shows disagreement at  $h\nu > 1000$  eV and confirms that the spectral shape of the heating radiation modeled in detail cannot be reproduced by a single Planckian distribution. FIG. 6(b) shows the spectral irradiance calculated for the *Thick CH* ( $h = 1.4 \pm 0.1$  mm) case at  $t = -2, -1, 0, +1,$  and  $+2$  ns with respect to the time of the backlight-radiation peak. The heating radiation changes both its brightness and its spectral shape throughout time. The heating-radiation calculation is repeated for the *Thin CH* ( $h = 2.2 \pm 0.2$  mm) and *CH+Be* ( $h = 1.5 \pm 0.1$  mm) cases. FIG. 6(c) shows the heating-irradiance time history simulated for each target configuration. Since the result confirms that the source-to-sample distance strongly influences the sample heating as suggested in Ref. [28]. The heating-radiation calculation also suggests that the heating-irradiance peak occurs between the total axial radiation power peak measured by XRDs and the modeled backlight-radiation peak for all the three tamper configurations.

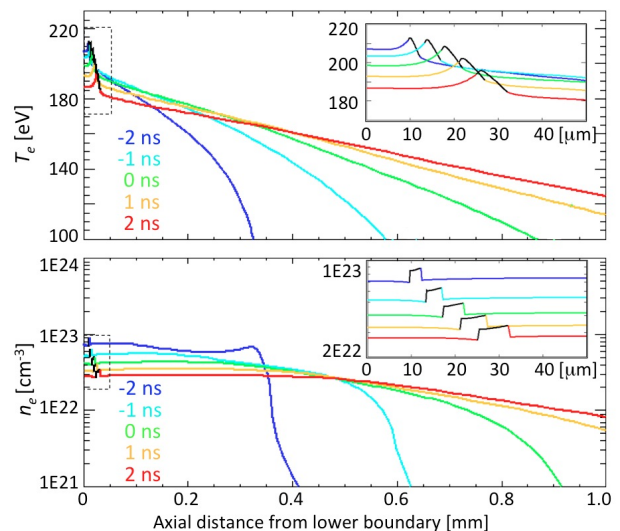


FIG. 7. (Color online) (a)  $T_e$  and (b)  $n_e$  axial profiles simulated for the *Thick CH* case at  $t = -2, -1, 0, +1,$  and  $+2$  ns with respect to the backlight radiation peak. The dashed-rectangle range is blown up in the upper right corner to better show the FeMg sample region indicated by black lines.

## B. Modeling sample/tamper hydrodynamics

We use the 1-D Lagrangian hydrodynamic code HELIOS [29, 30] to simulate the sample/tamper axial plasma evolution. The primary goal of the HELIOS simulation is to produce reasonable  $T_e$  and  $n_e$  axial profiles and their time histories that approximate those of the Z experiments. One challenge is the effect of the ZPDH CH<sub>2</sub> plasma on the sample/tamper hydrodynamics [21].

The ZPDH plasma affects the sample hydrodynamics in two ways: 1) providing heating radiation and 2) providing upward mechanical pressure. The first effect is discussed and taken into account in Sec. III A.

The second effect, upward pressure, is physically provided by the ZPDH CH<sub>2</sub> plasma. To approximate upward-pressure effects and better simulate the sample density time history, we restricted the heating radiation to  $t > -3$  ns (FIG. 6) with respect to the backlight-radiation peak. Furthermore, the boundary of the lower CH tamper surface is fixed at its initial location so that the sample is prevented from expanding downward. This ad-hoc treatment effectively corrects the sample-expansion onset without altering the sample  $T_e$  time history because the sample  $T_e$  at  $t$  is determined mostly by the heating radiation at that time. The limitation due to the drive onset adjustment is discussed in Sec. IV.

HELIOS simulations are performed to approximate the hydrodynamics of eight experiments: two Fe thicknesses for the *Thin CH* configuration, three for the *Thick CH*, and three for the *CH+Be*. Here, we use a subset of results to visualize the plasma hydrodynamics in terms of axial and temporal gradients of  $T_e$  and  $n_e$ .

FIG. 7 shows  $T_e(z)$  and  $n_e(z)$  at  $t = -2, -1, 0, +1,$  and

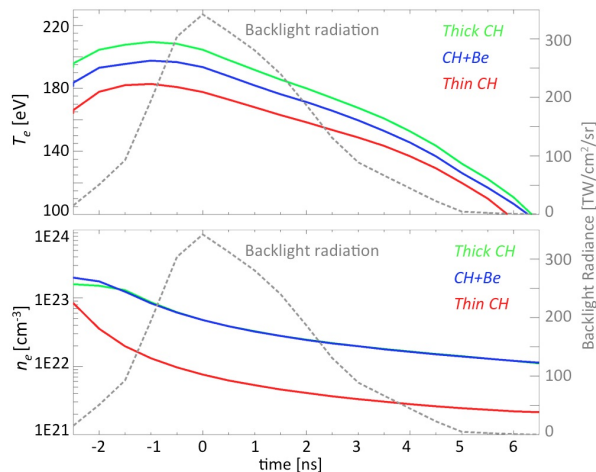


FIG. 8. (Color online) Simulated  $T_e$  and  $n_e$  temporal profiles at the center of the sample for the *Thick CH* (green), *CH+Be* (blue), and *Thin CH* (red). The different tamper configurations produce different sample hydrodynamics.

+2 ns simulated for the FeMg embedded in the *Thick CH* configuration. The black regions indicate the FeMg-embedded regions while the colored regions indicate the CH-tamper regions. The axial  $T_e$  gradient in the FeMg sample is small (<10%) for all simulations. There are much larger gradients in the top tamper at each time due to the free expansion of the observer side. We confirmed that various Fe thicknesses with the same tamper configuration showed very similar hydrodynamics.

FIG. 8 shows  $T_e(t)$  and  $n_e(t)$  from the central zone of the FeMg-embedded regions simulated for the *Thin CH* (red), *Thick CH* (green), and *CH+Be* (blue) tamper configurations, respectively. As expected from the simulated heating radiation in FIG. 6(b), the *Thin CH* tamped sample reached lower temperature than those of the *Thick CH* and *CH+Be* tamped samples due to its larger distance to the radiation source, and it also reached significantly lower  $n_e$  due to smaller top-tamper mass and less tamping pressure. The gray dashed line is the backlight radiance time history (Sec. V A), and we infer that  $T_e$  drops about 13-14% and  $n_e$  drops roughly by 70% over the backlight full-width-at-half-maximum.

To confirm that our simulations are reasonable, we show that the characteristic conditions are consistent with our measurements. For each hydrodynamic simulation result,  $T_e(t, z)$  and  $n_e(t, z)$  are post-processed to simulate FeMg spectral images as discussed in Sec. III C. Examples of the spectral lineouts extracted from the simulated image data are shown in FIG. 9. Solid and dashed curves are those extracted from  $+9^\circ$  and  $-9^\circ$  images, respectively. The Mg lines of the solid curves from the *CH+Be* and *Thick CH* cases are broader than those from the *Thin CH* case, which is a spectroscopic signature that the *CH+Be* and *Thick CH* cases achieved higher density in FeMg plasmas. For more quantitative comparisons, the effective FeMg plasma conditions are inferred by an-

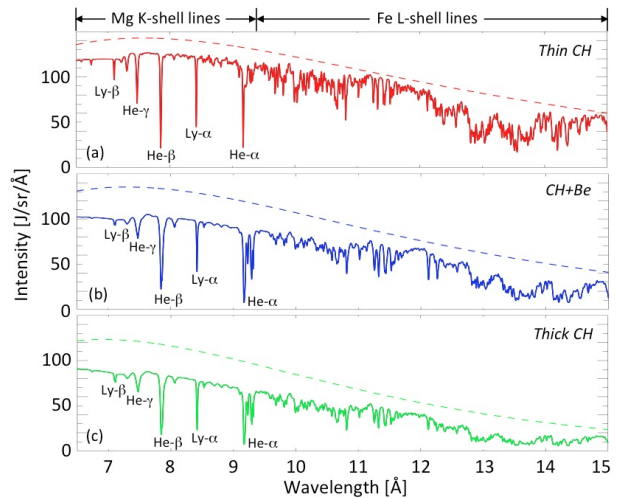


FIG. 9. (Color online) Spectra extracted from the simulated half-moon data for  $\pm 9^\circ$  spectrometers for (a) *Thin CH*, (b) *CH+Be*, (c) *Thick CH* tamper configurations. Spectra extracted at the bright spots on the image data (FIG. 13) result in FeMg-attenuated (solid) and unattenuated (dashed) spectra. Strong line features at  $\lambda < 9.5$  Å are Mg K-shell lines such as He- $\alpha$ ,  $\beta$ ,  $\gamma$  and Ly- $\alpha$ ,  $\beta$  lines, while lines at  $\lambda > 9.5$  Å are absorption features due to Fe L-shell lines.

alyzing the Mg lines in the same way as discussed in Ref. [8].

FIG. 10 compares the conditions inferred from the measured (black squares) and simulated data (red circles), confirming very good agreement. The differences in the simulations are the target configurations defined in the HELIOS simulations and the source-to-sample distances used in the heating-radiation calculations. We note that there are two free parameters: i) calibration factor for the ZPDH intensity images to account for intensity increase after the refurbishment and ii) heating-radiation onset time to avoid the artificial early sample expansion. It is encouraging that HELIOS simulations with the same parameters (i.e., calibration factor = 2.6, onset time = -3 ns) systematically reproduce the measured conditions within the measurement uncertainties for all the experiments.

### C. Modeling Z sample-transmitted image data

Once plasma  $T_e(t, z)$  and  $n_e(t, z)$  are simulated with HELIOS, we compute spectral images on the detector plane by performing radiation transport through the simulated sample with the local-thermal equilibrium (LTE) emissivity and opacity database. The database is computed with PrismSPECT [31], which produces similar spectra to the opacity models in Ref. [9]; its Fe spectrum is in good agreement with the data at  $T_e = 156$  eV and  $n_e = 6.9 \times 10^{21} \text{ cm}^{-3}$  [7], while it exhibits discrepancies similar to other models at higher  $T_e$  and  $n_e$ . While the post-processing can be done with any other

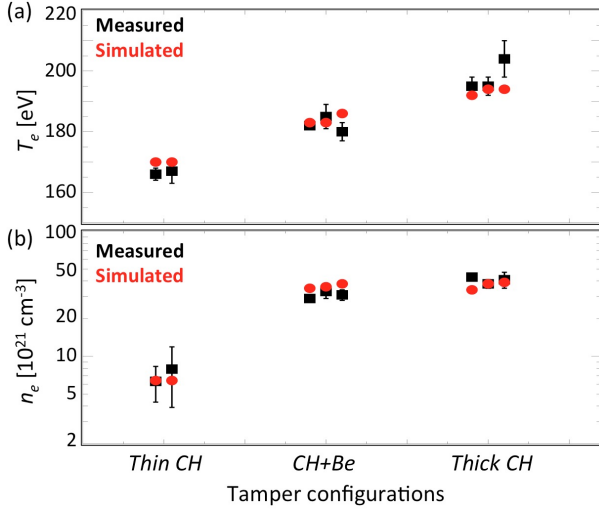


FIG. 10. (Color online) HELIOS hydrodynamic simulations are performed for existing data with various target configurations. There are several Fe thicknesses for each tamper configuration. (a)  $T_e$  and (b)  $n_e$  values inferred from the simulated spectra agree well with the conditions inferred from the measured spectra.

spectral models, PrismSPECT is selected due to its user-friendliness, flexibility, and availability.

### 1. Radiation transport through the target

Calculating detailed radiation transport through the gradients simulated in Sec. III B is critical to accurately understand our measurements. As discussed in Sec. III A, modeling radiation observed at any given point in space is difficult in general due to complicated spatial integration involving 3-D view factors between the radiating surface and the observer. However, the fact that the detector is located very far from both the sample plasma and the radiation source simplifies the 3-D view-factor calculation. As a result, the spectral image can be simulated as follows (see Appendices A and B for details):

$$I^{\text{image}}(\nu, x'') = \int I^{\text{image}, t}(\nu, x'') dt \quad (2)$$

$$I^{\text{image}, t}(\nu, x'') dt = A \cos \theta \left\{ \tilde{T}_\nu^t \tilde{B}_\nu^t(x'') + \tilde{J}_\nu^t \right\} dt \quad (3)$$

where  $I^{\text{image}}(\nu, x'')$  and  $I^{\text{image}, t}(\nu, x'')$  are simulated time-integrated and time-resolved spectral images at time  $t$ , respectively.  $A$  is the area of the source observable through the aperture and the slits from a point  $x''$  on the detector.  $\tilde{B}_\nu^t(x'')$  is the backlight radiation observed at film spatial point  $x''$  taking into account the finite slit spatial resolution as defined in Eq. (16).  $\tilde{T}_\nu^t$  and  $\tilde{J}_\nu^t$  are

the net plasma transmission and emerging plasma self-emission taking into account the finite spectral resolution of the instruments as defined in Eqs. (20) and (21). The tilde indicates that the instrumental broadening is taken into account [Eqs. (20) and (21)].

Plasma axial gradients simulated in Sec. III B affect  $T_\nu^t$  and  $J_\nu^t$ , and thus they have to be computed in detail by numerically solving radiation transport through the simulated plasma axial-condition profiles:

$$T_\nu^t = \prod_{i=1}^N T_{\nu, i}^t, \quad T_{\nu, i}^t = e^{-k_{\nu, i}^t L_i^t}$$

$$J_\nu^t \equiv J_{\nu, N}^t$$

where

$$J_{\nu, i}^t = J_{\nu, i-1}^t e^{-k_{\nu, i}^t L_i^t} + \frac{j_{\nu, i}^t}{k_{\nu, i}^t} \left( 1 - e^{-k_{\nu, i}^t L_i^t} \right), \quad i = 1 \dots N \quad (4)$$

$$j_{\nu, i}^t = \sum_m n_{\text{ion}, i}^t f_i^m \epsilon_\nu^m(T_{e, i}^t, n_{e, i}^t) \quad (5)$$

$$k_{\nu, i}^t = \sum_m n_{\text{ion}, i}^t f_i^m \kappa_\nu^m(T_{e, i}^t, n_{e, i}^t) \quad (6)$$

where  $J_{\nu, i}^t$  is the emergent plasma emission at the end of axial zone  $i$ .  $i = 1$  is the radiation-source side, and  $i = N$  is the observer side.  $L_i^t$  is the size of axial zone  $i$  at time  $t$ .  $j_{\nu, i}^t$  and  $k_{\nu, i}^t$  are, respectively, the mixture emissivity in erg/s/cm $^2$ /sr/eV and the mixture absorption coefficient in cm $^{-1}$  of zone  $i$  at time  $t$ .  $j_{\nu, i}^t$  and  $k_{\nu, i}^t$  can be computed from the atomic number fraction of element  $m$  at zone  $i$ ,  $f_i^m$ , the databases of the element fractional emissivity,  $\epsilon_\nu^m$ , and element fractional absorption coefficient (or, absorption cross-section),  $\kappa_\nu^m$ , that are computed with PrismSPECT [31], and the conditions of zone  $i$  at time  $t$  (i.e.,  $T_{e, i}^t$ ,  $n_{e, i}^t$ , and total ion density,  $n_{\text{ion}, i}^t$ ) [8]. Thus, the spectral image at time  $t$  can be computed from the hydrodynamic-simulation results (i.e.  $T_{e, i}^t$ ,  $n_{e, i}^t$ ,  $n_{\text{ion}, i}^t$ , and  $L_i^t$ ; Sec. III B), the calibrated backlighter image at time  $t$  [i.e.,  $B_\nu^t(x', y')$  in Eq. (16)], and the local-thermodynamic-equilibrium (LTE) fractional element emissivity and opacity databases discussed in Ref. [8].

### 2. Comparison of the simulated and measured spectral images

To verify the spectral image modeling, we selected the simplest case: on-axis *Thin CH* tamper-only data. FIG. 11(a) and (b) show the simulated spectral image at  $t =$

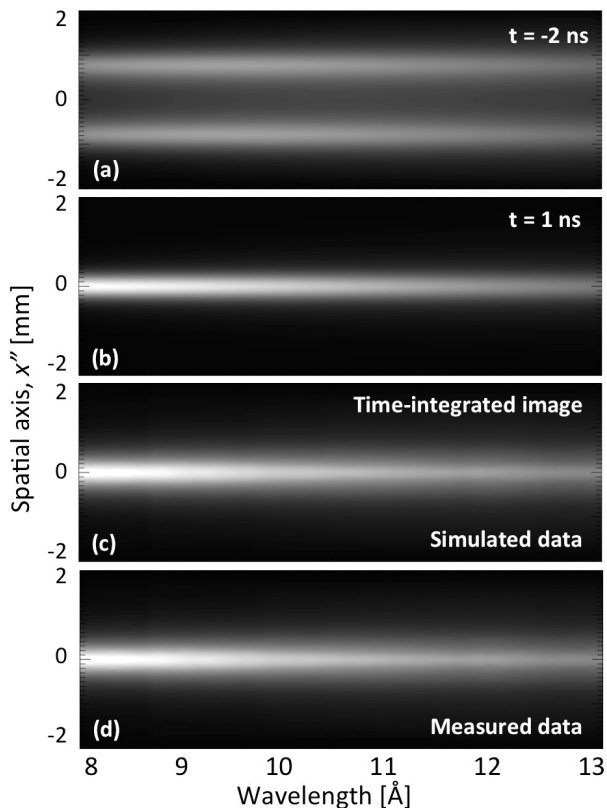


FIG. 11. Simulated spectral image for the *Thin CH* tamper-only case at (a)  $t = -2$  ns and (b)  $t = 1$  ns, and (c) time-integrated. (d) is the measured spectral image averaged over five data set. The backlighter spectral images simulated (c) and measured (d) at  $0^\circ$  show very good agreement.

- 2 ns and 1 ns, respectively. One can observe that FIG. 11(a) shows radiative shock fronts around  $\pm 1$  mm; they collide on axis (i.e.,  $x'' = 0$ ) at  $t = 1$  ns as shown in FIG. 11(b). The x-ray film accumulates the signals over the entire experiment duration. Thus, the time-integrated image shown in FIG. 11(c) represents the simulated spectral image, which is qualitatively identical to the measured spectral image obtained with a spectrometer located at  $0^\circ$  shown in FIG. 11(d).

For quantitative comparisons, spectral and spatial profiles are extracted both from the simulated (red) and the measured spectral images (black) and plotted in FIG. 12(a) and (b), respectively. The spectra are extracted at the apparent stagnation point on the detector (i.e., bright spot) over  $0.3$  mm, and the spatial profiles are extracted at  $\lambda = 9.0$  Å over  $0.1$  Å. The gray dashed curves account for the experiment-to-experiment reproducibility that reflects the variations in backlight radiation, uncalibrated crystal reflectivity, x-ray film sensitivity, and slit width. These standard deviations are not large considering the fact that they are calculated over five data sets taken over two years with multiple different spectrometers with different crystals. The experiment-to-experiment variation in backlight radiation alone should

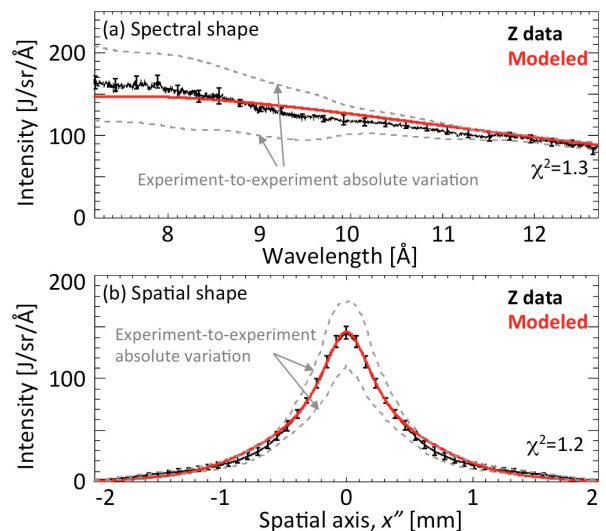


FIG. 12. (Color online) Comparison in (a) spectral and (b) spatial profiles extracted from the simulated (red) and the measured (black) image data. The spectral profiles are extracted at the brightest spot over  $0.3$  mm. The spatial profiles are extracted at  $9$  Å over  $0.1$  Å. Gray dashed curves indicate experiment-to-experiment absolute variations, which includes variations in backlight brightness, uncalibrated crystal reflectivity, x-ray film sensitivity, and slit width over five data sets in two years. Black error bars show the standard deviations in the relative shapes. The reduced  $\chi^2$  are computed based on the relative shapes.

be much smaller. The reproducibility in measured conditions indirectly suggests this point since the variation in the ZPDH radiation should affect not only the backlight radiation but also the sample heating radiation [8]. The relative shapes are more reproducible over experiments, which are shown as black error bars in the figures. The data-model comparisons confirm that the simulated spectral image agrees with the measured one both in brightness and in shapes within the measurement uncertainties.

There are several approximations in the simulations. We start with ZPDH radiation intensity images recorded before the Z-facility refurbishment. To account for intensity increases due to the refurbishment, the image intensity is scaled by 2.6 so that the simulated conditions agree with the measured conditions (FIG. 10). Also, we assume that every point of the ZPDH image emits a single Planckian of different temperatures and that the backlighter brightness and shape can be accurately computed by integrating spectral irradiance over the observable ZPDH area [Eq. (16)]. The radiation transport through the  $20\text{-}\mu\text{m}$  CH, view factors, aperture, and slits is then taken into account [Eqs. (2)-(6)]. The quantitative agreement shown in FIG. 10 – 12 supports the soundness of these approximations in the simulations.

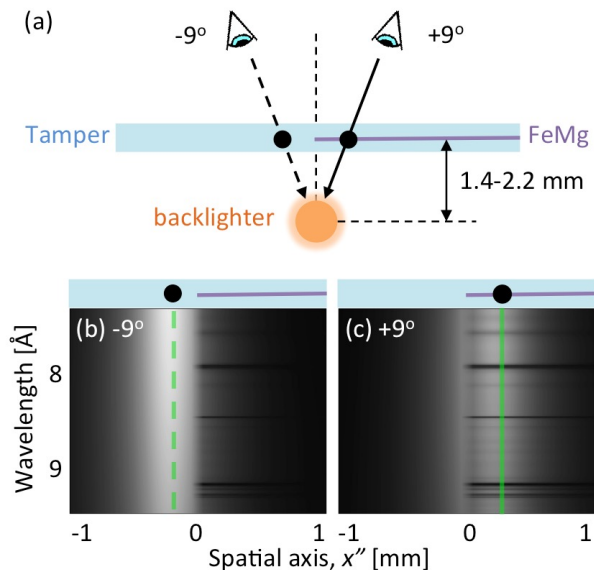


FIG. 13. (Color online) (a) Schematics to illustrate the lateral shift in apparent backlighter bright spot on the  $\pm 9^\circ$  image data. Images are not to scale. (b) and (c) illustrate the simulated *Thick CH* half-moon data at  $-9^\circ$  and  $+9^\circ$ , respectively. Green solid and dashed lines indicate location of backlighter spatial intensity maximum (i.e., black filled circles in the schematics).  $x = 0$  is defined to correspond to the FeMg boundary. The images in (b) and (c) are restricted to the 7 – 9.5 Å range for clarity.

### 3. Modeling half-moon spectral images at $\pm 9^\circ$

The same algorithm is employed to simulate half-moon spectral images for the  $\pm 9^\circ$  line of sight (LOS) but taking into account the relative lateral shift between the backlighter bright spot and the half-moon boundary that arises due to the parallax. FIG. 13 (a) illustrates this point. Due to the 1.4–2.2 mm source-to-sample distance,  $h$ , the spectrometer at  $+9^\circ$  sees the backlighter bright spot shifted to the FeMg-embedded side by  $h \tan 9^\circ$ , while the spectrometer at  $-9^\circ$  finds the bright spot on the tamper-only side, shifted by  $-h \tan 9^\circ$ . The resultant Z image data at  $\mp 9^\circ$  simulated for the *Thick CH* half-moon case are shown in FIG. 13 (b) and (c), respectively. The images are rotated by  $90^\circ$  so that the reader can relate the spatial axis in the schematic diagram with those in the images.

We typically extract FeMg-attenuated and -unattenuated spectra at the brightest spots of  $\pm 9^\circ$  images, which are indicated by green solid and dashed lines in FIG. 13 (c) and (b), respectively. The extracted spectra are shown in FIG. 9(c). The same simulations are repeated for the *Thin CH* and *CH+Be* cases, and the extracted spectra are shown in FIG. 9(a) and (b), respectively.

## IV. LIMITATIONS

### A. Calibrating the pre-refurbished ZPHD radiation source

The simulations rely on the measured 2-D space-resolved ZPHD radiation time history (Sec. III A). Since we have not updated the measurements of gated pinhole images and radiation power time history for the refurbished ZPHD, we use those data available from before the refurbishment to initiate the simulations. To account for the intensity increase due to the refurbishment, we scaled the intensity values by 2.6.

We note that the calibration factor of 2.6 produces an output radiance that is approximately 20-40% higher than the expected radiation output (the exact output from the refurbished Z has not yet been measured, as we pointed out above). While the formal interpretation of this number requires further investigation and is beyond the scope of this article, this difference is qualitatively consistent with the measured/modeled opacity discrepancies in Ref. [9]. If the calculated Fe opacity were indeed significantly lower than the true value, then the radiation output in the simulation that is required to drive the sample to the measured temperature will be higher than the true radiation output. However, the lack of the full characterization of the refurbished ZPHD radiation is a limitation of the current simulations. We are working on updating the pinhole images and radiation-power time-history measurements.

### B. Potential inaccuracy in top-tamper hydrodynamics

While the simulated sample conditions are validated with the measured conditions, the simulated top-tamper hydrodynamics may not be as accurate as the FeMg sample for two reasons. First, geometrical dilution is calculated at the measured source-to-sample distance [28]. However, as FIG. 7 illustrates, the top tamper extends over a wider axial dimension and farther from the source. Thus, using heating radiation calculated at the sample location would underestimate the geometrical dilution and overestimate the heating at the far side of the top tamper. This is a limitation of the 1-D hydrodynamics code. Space-dependent geometrical dilution would be the most important 2-D/3-D effect when the geometrical dilution of the drive radiation significantly changes over the target volume. We note that this problem is not as serious for the bottom tamper because it remains closer to the FeMg sample due to the smaller initial thickness and the smaller expansion.

Second, the truncation of early-time radiation is introduced to approximate the delay of the sample expansion onset due to the the upward acceleration of the bottom boundary. However, early-time expansion may be happening on the top of the target. If this is the case, the

artificial truncation of the heating radiation would underestimate the expansion and overestimate the density of the top-tamper region.

Thus, due to these limitations, the simulated hydrodynamics probably overestimate  $T_e$  and  $n_e$  for a portion of the top tamper. At the moment, we assume that, since both  $T_e$  and  $n_e$  should be lower, discrepancies in mean charge are not as large as the discrepancies in  $T_e$  and  $n_e$  themselves. Also, the tamper material and thickness are selected to minimize their radiative effects on the measurements. Thus, we also assume that the impact of the discrepancies in the top-tamper hydrodynamics is minimal. It is important to keep in mind these limitations when numerically quantifying the impact of tamper effects on our measurements.

### C. 1-D hydrodynamics

The present work investigates axial hydrodynamic effects on our opacity measurements. We neglect any 2-D/3-D effects. Consequently, the sample lateral gradient is neglected assuming the sample  $T_e$  and  $n_e$  slowly change in the lateral direction compared to the steep lateral intensity gradient of the backlight radiation shown in FIG. 2. This is a reasonable assumption considering the heating radiation characteristics. Two lateral points on the sample see exactly the same radiation source except for the view factor; however, the view factor changes by a small amount ( $< 5\%$ ) over the observable area. If the sample lateral gradients turn out to be more important, the averaged self-emission would be weaker and the self-emission effects on the measured spectra would be even smaller.

We also assume that ZPDH plasma pressure is strong enough that it prevents the sample from expanding downwards, and we therefore fix the bottom boundary in the simulation at the measured distance. If this assumption is incorrect, the true time dependent spectral irradiance at the sample will be different from the simulation values [32]. However, our use of calibration method that forces the simulations to reproduce the  $T_e$  and  $n_e$  at wide variety of different samples should minimize the impact.

### D. Steady-state LTE atomic kinetics

The emissivity and opacity databases discussed in Sec. III C are solved in steady-state LTE. The time-dependent effects are assumed to be negligible because the hydrodynamics time scale is sub-ns and assumed to be long enough for the high-density (or collision-dominated) population kinetics to rapidly reach the steady-state solution. To quantify the importance of non-LTE effects, the non-LTE population is computed at the center of the FeMg sample at each temporal point with PrismSPECT using the heating radiation modeled in Sec. III A. The deviation in the mean charge from the LTE case is  $< 2\%$ .

## V. DISCUSSION

We presented a calibrated simulation to better bridge the static-uniform picture used in the data interpretation to the dynamic-gradient reality in the experiments. The sample conditions inferred from the simulated data agree with the measured conditions reported in Ref. [8, 9] for eight experiments. The image formation algorithm is supported by quantitative agreement of the modeled/measured backlighter spectral images. Such practical simulations not only help refine our understanding of the backlight-radiation time history and sample heating, but also become powerful tools to quantify potential systematic errors in the data interpretation.

### A. Backlight-radiation time history

Understanding the time history of the backlight radiation is not straightforward for the SNL opacity experiments because the backlight radiation is provided by spatially dependent ZPDH source radiation that propagates through an aperture and slits. In Sec. III C 2, simulated FeMg-attenuated and -unattenuated spectra are extracted by integrating the brightest 0.3-mm region vertically along the simulated spectral images. We take spectral lineouts at this brightest region not only because that provides the best signal-to-noise ratio, but also because that would maximize the backlight-to-self-emission contrast, thus minimizing the plasma self-emission effects. Since we have simulated the spectral image for the experiments without the FeMg sample and accounted for effects of the aperture and slits, we can learn the backlight radiation time history from the time-resolved spectral images of such simulations.

The 0.3-mm spectral lineouts are extracted at the stagnation point of the spectral images simulated at  $t = -2, -1, 0, 1,$  and  $2$  ns and shown in FIG. 14. The backlight spectral intensity changes its brightness and spectral shape over this duration. The backlight-brightness time history is extracted by integrating these spectra over the spectral range of the measurement (red curve in FIG. 4). The backlight brightness peaks later than the XRD power peak (FIG. 4) or the heating-radiation peak (FIG. 6). While the sample is exposed to the radiation emitted from the whole ZPDH (FIG. 2), the stagnation point on the detector collects the radiation from only the central  $0.3 \times 1.0 \text{ mm}^2$  of the ZPDH source due to the aperture and slits (FIG. 16). Since the backlight radiation peaks after the heating radiation, the ZPDH radiation backlights the sample when it is slowly cooling [FIG. 6(c)]. Its characteristic time and duration are determined based on the median and central 68% of the brightness time history and found to be at 0.5 ns and over 3.0 ns, respectively.

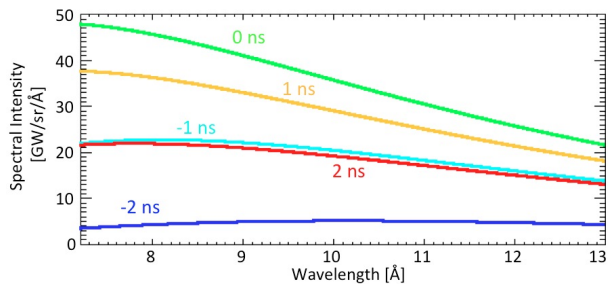


FIG. 14. (Color online) Spectra taken at  $x'' = 0$  (i.e., ZPDH stagnation point) from simulated time-resolved spectral image for *Thin CH* tamper-only data at  $t = -2, -1, 0, 1,$  and  $2$  ns.

### B. Sample heating

Mg K-shell spectroscopy demonstrated that samples with different tamper configurations reached different temperatures and densities [8]. Previous simulations predicted that the sample density should increase with tamper mass because the tamper slows the sample upward expansion [24]. However, it was a surprise to find that the heavier tamper also produced higher sample temperatures. Recently, a strong anti-correlation between the sample temperatures and source-to-sample distances was found from parallax measurements [28]. This led to a hypothesis that the higher temperatures arose because the heavier top tamper inhibits upward sample bulk motion (away from the source). This allows the sample to remain closer to the heating radiation and reach higher temperatures than those with the lighter top tamper. The new simulations developed here provide additional insight to this hypothesis.

The source-to-sample distances measured by parallax for the *Thin CH*, *CH+Be*, and *Thick CH* are  $2.2 \pm 0.2$ ,  $1.5 \pm 0.1$ , and  $1.4 \pm 0.1$  mm, respectively. These distances must be the sum of three contributions: i) the distance between the source and the initial location of the target, ii) the distance traveled by the lower boundary of the bottom tamper due to upward mechanical pressure provided by the ZPDH plasma, and iii) the expansion of the bottom tamper. i) is not the source of the parallax differences because the targets are placed at the same location and the ZPDH radiation is nominally identical. The parallax differences have to be produced by the distance traveled from the initial location due to the sample motion and the bottom tamper expansion.

The simulated bottom-tamper expansion for *Thin CH*, *CH+Be*, and *Thick CH* targets at the characteristic time of the backlighter (i.e., the median of the backlight time history discussed in Sec. V A) are 0.53, 0.11, and 0.02 mm, respectively. Analyzing the differences between the *CH+Be* and *Thick CH* simulations provide insight into the sample heating control. The tampers of the *CH+Be* and *Thick CH* targets have roughly the same mass. Thus, the ZPDH plasma should push both targets approximately the same distance from the initial location.

In fact, the difference in the lower-boundary-to-sample distance (i.e.,  $0.11 - 0.02 \approx 0.1$  mm) explains the relative distance observed by the parallax measurements (i.e.,  $1.5 - 1.4 = 0.1$  mm). It follows that their lower-boundary locations are approximately the same at the backlight time. Therefore, this suggests that the *CH+Be* case did not achieve as high temperature as the *Thick CH* case because FeMg samples in *CH+Be* targets reached 0.1 mm farther away from the source due to the extra thickness and expansion of the bottom tamper. This suggests that, by reducing the bottom-tamper thickness of the *CH+Be* target to  $2 \mu\text{m}$ , its sample temperature will increase and become as hot as those of *Thick CH* targets.

Comparison of the bottom-tamper expansion difference between the *CH+Be* (0.11 mm) and *Thin CH* (0.53 mm) provides an additional insight. While they initially have the same bottom-tamper material and thickness, the *CH+Be* bottom-tamper expands much less due to the extra  $35\text{-}\mu\text{m}$  Be mass on the top. Due to this extra mass, the bottom tamper expansion was limited to  $1/5$  of the *Thin CH* bottom tamper. Also, the bottom-tamper expansion difference, 0.42 mm, does not fully explain the observed sample location difference, i.e.,  $2.2 - 1.5 = 0.7$  mm. This suggests that the lower boundary of the *Thin CH* target is pushed 0.3 mm farther up than that of the *CH+Be* due to the overall mass difference. The 1-D simulations together with the parallax measurements and the sample condition measurements significantly improve our understanding of the sample heating.

### C. Synthetic investigations of systematic measurement errors

The simulated data discussed here contain many details that are neglected in the data interpretation, such as the effects of integration over temporal/axial gradients, self-emission, and the tamper, and the analysis of these simulated data supported the conclusion that the opacity discrepancies observed between opacity models and the measurements cannot be explained by these systematic errors in the measurements [9]. Details will be discussed in subsequent papers.

### ACKNOWLEDGEMENT

We thank the Z-facility teams for invaluable and dedicated technical assistance. We also thank R. W. Lee and S. B. Hansen for their expertise and useful discussion and R. E. Falcon for refining the manuscript. Sandia is a multiprogram laboratory operated by Sandia Corporation, a Lockheed Martin Company, for the United States Department of Energy under contract DE-AC04-94AL85000.

## APPENDIX A: MODELING OBSERVED RADIATION

Modeling observed radiation is often a complicated calculation requiring spatial integration involving 3-D view factors. FIG. 15 (a) shows an example of a detector observing radiation from a point of an emitting surface. We focus on radiation observed by a small surface,  $s$ , of the detector, which can be written as:

$$J_\nu^t(x, y) \Omega(x, y) \cos \theta(x, y) \quad [\text{erg/s/cm}^2/\text{eV}] \quad (7)$$

where  $J_\nu^t(x, y)$  is the spectral radiance of the emission surface at point  $(x, y)$  at time  $t$  [erg/s/cm<sup>2</sup>/sr/eV],  $\Omega(x, y)$  is the solid angle from the point  $(x, y)$  to the surface,  $s$ , in steradians, and  $\cos \theta(x, y)$  comes from the Lambertian emitter assumption. The total radiation per detector unit area can be computed by integrating Eq. (7) over the whole emitting area,  $A$ , divided by the area of the surface,  $s$ :

$$\iint_A J_\nu^t(x, y) \frac{\Omega(x, y)}{s} \cos \theta(x, y) dx dy \quad [\text{erg/s/cm}^2/\text{eV}] \quad (8)$$

Note that both Eqs. (7) and (8) have the same units. However, 1/cm<sup>2</sup> refers to per-source-area in Eq. (7), while it refers to per-detector-area in Eq. (8). Also, the quantity  $\Omega(x, y)/s$  represents the solid angle per detector unit area, which can be uniquely determined by source-to-detector distance and crystal geometry.

Radiation observed from a plasma with backlight radiation can be modeled as a two-sheet plasma as shown in FIG. 15 (b). By elaborating upon Eq. (8), the time-integrated radiation observed at a point on the detector is:

$$I_\nu = \int I_\nu^t dt = \int \{X_\nu^t + Y_\nu^t\} dt \quad [\text{erg/cm}^2/\text{eV}] \quad (9)$$

$$X_\nu^t = \iint_A J_\nu^t(x, y) \frac{\Omega(x, y)}{s} \cos \theta(x, y) dx dy \quad (10)$$

$$Y_\nu^t = \iint_{A'} T_\nu^t(x, y) B_\nu^t(x', y') \frac{\Omega(x', y')}{s} \times \cos \theta(x', y') dx' dy' \quad (11)$$

where  $X_\nu^t$  and  $Y_\nu^t$  are the space-integrated plasma self-emission and plasma-transmitted backlight radiation per detector unit area at time  $t$ ,  $J_\nu^t(x, y)$  and  $B_\nu^t(x', y')$  are the spectral radiance of the plasma self-emission and the backlighter at time  $t$ ,  $(x, y)$  and  $(x', y')$  are points on the self-emission surface and the backlighter surface, respectively, and  $T_\nu^t(x, y)$  is the transmission of the plasma at time  $t$ , where the point  $(x, y)$  in interest is a function of  $(x', y')$  for a given point on the detector. As shown by these equations, modeling radiation observed by a point in space is quite involved even for a simple two-sheet plasma picture due to the space-dependent

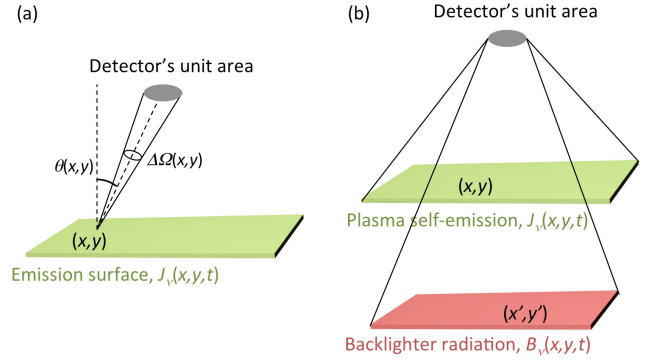


FIG. 15. (Color online) (a) Radiation contributed from a point on an emission surface depends on the view factor  $\Omega(x, y) \cos \theta(x, y)$ . (b) Schematic illustrating self-emission and backlighter radiation contributing to the infinitesimally small surface,  $s$ , on the detector.

view factors  $\Omega(x, y) \cos \theta(x, y)$  and  $\Omega(x', y') \cos \theta(x', y')$ . However, when the detector is located very far from the backlighter radiation source and the self-emission plasma, these equations are simplified. The next section discusses modeling of the Z spectral image by simplifying these equations with approximations.

## APPENDIX B: MODELING Z DATA

The spectral image measured with the space-resolved spectrometers [e.g., Fig. 11(d)] can be modeled by solving for  $I_\nu$  of Eq. (9) at every spatial point on the film. In this section, the procedure of spectral image modeling is discussed for an example of the *Thin-CH*-tamper-only experiment measured along the axis.

FIG. 16 (a) illustrates that each spatial point  $x''$  on film observes radiation integrated over a  $0.1 \text{ mm} \times 1.0 \text{ mm}$  rectangle limited by the aperture and slits above the sample. The slits are located halfway to the detector, which provides a magnification of 1 and simplifies the interpretation of the data. A different spatial point  $x''$  on film measures radiation integrated over a different  $0.1 \text{ mm} \times 1.0 \text{ mm}$  rectangle centered at  $x = x''$ . While the calculation of  $I_\nu$  discussed in Appendix A is quite involved due to the space-dependent 3-D view factors, the formula can be simplified by introducing two approximations valid for our experiments.

First, since the detector is far from the sample ( $\sim 4180 \text{ mm}$ ), the view-factor difference across the observable area of the source [e.g., the red rectangle in Fig. 16 (a)] is negligible. As a result, we can employ the following approximation:

$$\frac{\Omega(x, y)}{s} \cos \theta(x, y) = \frac{\Omega(x', y')}{s} \cos \theta(x', y') = \frac{\Omega}{s} \cos \theta. \quad (12)$$

Also, the source-to-sample distance is very small compared to the source-to-detector distance, which makes

$x' = x, y' = y$ . For both the plasma and the backlighter, the observable emitting areas are limited by the aperture and slits, which makes  $A = A'$ .

Another approximation introduced in the data modeling is the assumption that the plasma conditions are laterally uniform:

$$J_\nu^t(x, y) = J_\nu^t. \quad (13)$$

Since each point in the plasma observes all the radiation, the heating radiation across the sample does not change as dramatically as the source-radiation spatial distribution (i.e.,  $B_\nu^t(x, y)$ ). By introducing these two approximations,  $X_\nu$  and  $Y_\nu$  can be simplified to:

$$X_\nu^t(x'') = \frac{\Omega}{s} \cos \theta A J_\nu^t \quad (14)$$

$$Y_\nu^t(x'') = \frac{\Omega}{s} \cos \theta A T_\nu^t \tilde{B}_\nu^t(x'') \quad (15)$$

$$\tilde{B}_\nu^t(x'') \equiv \frac{1}{A} \int_{-w_a/2}^{w_a/2} \int_{x''/M-fw_s/2}^{x''/M+fw_s/2} B_\nu^t(x', y') dx' dy' \quad (16)$$

where  $\tilde{B}_\nu^t(x'')$  is an effective backlighter radiation at position  $x''$  at time  $t$ ,  $w_a$  is the aperture width (1.0 mm),  $w_s$  is the slit width (0.05 mm), and  $f = (1/M + 1)$ , which corrects the integration area if the magnification,  $M$ , is not exactly 1.  $A$  is the emitting area,  $A \equiv w_a \times fw_s$ , observable from a point on the detector,  $x''$ .

In our data processing, the data that originally have units of [photons/cm<sup>2</sup>] are converted into source radiation energy per solid angle [J/sr/Å] by correcting for curved KAP mosaic crystal reflectivity and film-position dependent filter transmissions, and by converting per-detector-area into per-source-solid-angle using film-position dependent  $\Omega/s$  determined taking into account the spectrometer geometry. Thus, to model such processed data, we need to compute  $I_\nu(x'')s/\Omega$  [erg/sr/eV] at every spatial position on the film with the approximations introduced above. Then, Eq. (9) becomes:

$$I^{\text{image}, t}(\nu, x'') = \int I^{\text{image}, t}(\nu, x'') dt \quad (17)$$

$$\begin{aligned} I^{\text{image}, t}(\nu, x'') &= \frac{s}{\Omega} I_\nu^t(x'') \\ &= A \cos \theta \left\{ T_\nu^t \tilde{B}_\nu^t(x'') + J_\nu^t \right\} \end{aligned} \quad (18)$$

where  $\Omega/s$  in  $I_\nu^t(x'')$  [see Eq. (9)-(11)] is cancelled out. After appropriate conversions from eV to Å and erg to J, Eqs. (17) and (18) are the time-integrated and instantaneous images of the simulated spectral image in [J/sr/Å] and in [J/s/sr/Å], respectively.

In addition to the spatial-integration effects due to the finite slit space resolution, one also has to take into account the instrumental spectral-resolution effects on the data. The instrumental-broadening profiles are previously measured using a Manson source [33]. They can be applied to the instantaneous image [Eq. (18)] as follows:

$$\begin{aligned} I^{\text{image}, t}(\nu, x'') &= \int g_{\nu'-\nu} A \cos \theta \\ &\quad \times \left\{ T_{\nu'}^t \tilde{B}_{\nu'}^t(x'') + J_{\nu'}^t \right\} d\nu' \\ &= A \cos \theta \left\{ \tilde{B}_\nu^t(x'') \int g_{\nu'-\nu} T_{\nu'}^t d\nu' \right. \\ &\quad \left. + \int g_{\nu'-\nu} J_{\nu'}^t d\nu' \right\} \\ &= A \cos \theta \left\{ \tilde{T}_\nu^t \tilde{B}_\nu^t(x'') + \tilde{J}_\nu^t \right\} \end{aligned} \quad (19)$$

where  $g_{\nu'-\nu}$  is an instrumental-broadening function centered at  $\nu$ .  $\tilde{B}_\nu^t(x'')$  is factored out from the convolution since the backlighter radiation is a smooth quasi-Planckian and can be approximated as constant over a narrow instrumental line profile,  $g_{\nu'-\nu}$ .  $\tilde{T}_\nu^t$  and  $\tilde{J}_\nu^t$  in the last equation are defined as:

$$\tilde{T}_\nu^t = \int g_{\nu'-\nu} T_{\nu'}^t d\nu' \quad (20)$$

$$\tilde{J}_\nu^t = \int g_{\nu'-\nu} J_{\nu'}^t d\nu'. \quad (21)$$

This derivation suggests two important points. First, after reasonable approximations, the Z-data simulation becomes simpler and more intuitive. At each time, one computes the emergent plasma self-emission,  $J_\nu^t$ , plasma transmission,  $T_\nu^t$ , and the effective backlighter image,  $B_\nu^t(x'')$ . The spectral-resolution effects are applied to  $J_\nu^t$  and  $T_\nu^t$  to produce  $\tilde{J}_\nu^t$  and  $\tilde{T}_\nu^t$ , and the spatial-resolution effects to  $B^t(x', y')$  to produce  $\tilde{B}_\nu^t(x'')$ . Then, the instantaneous spectral image can be simulated with Eq. (19). These images are integrated over time to simulate the time-integrated spectral image. Thus, at each time, one can check whether or not the self-emission is important by comparing  $X_\nu^t$  with  $Y_\nu^t$ . One can also check whether or not the net self-emission is important by comparing  $X_\nu$  with  $Y_\nu$ . Second, the derivation also suggests that, even after introducing the approximations discussed above, the temporal integration in Eq. (17) and the spatial integration for the effective backlighter in Eq. (16) have to be performed to reliably investigate the net plasma self-emission effects on the spectral image.

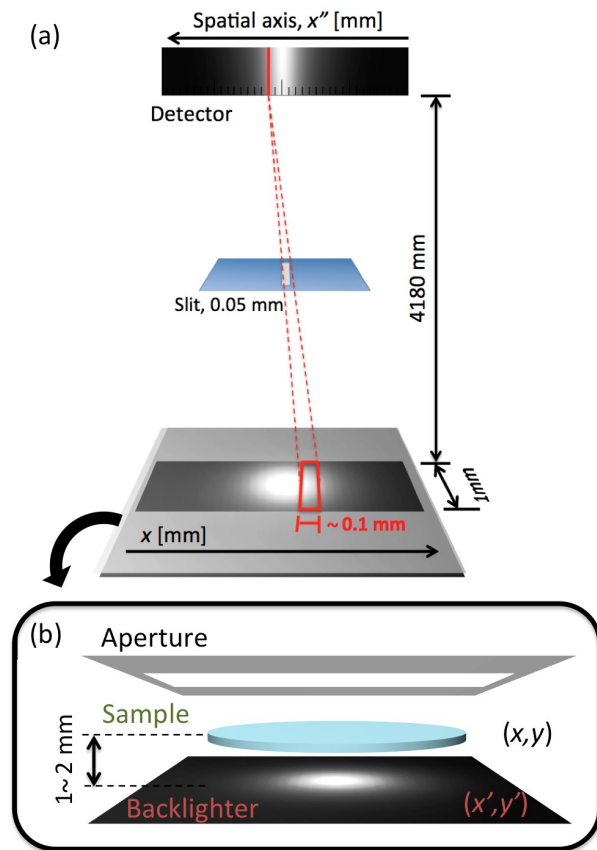


FIG. 16. (Color online) (a) Schematic illustrating how each spatial point on the film observes radiation through the aperture and slits. Each point in space observes radiation averaged over  $0.01 \times 0.1 \text{ mm}^2$  centered at  $x = x'$ . (b) Measured source-to-sample distance (1.4–2.2 mm) is much smaller than sample-to-detector distance (4180 mm). Schematics are not to scale.

- [1] D. Mihalas, *Stellar Atmospheres*, Astronomy and Astrophysics Series (W. H. Freeman, 1978).
- [2] S. Atzeni and J. Meyer-ter Vehn, *The Physics of Inertial Fusion: Beam-Plasma Interaction, Hydrodynamics, Hot Dense Matter: Beam-Plasma Interaction, Hydrodynamics*, International Series of Monographs on Physics (Clarendon Press, 2004).
- [3] R. P. Drake, *High-Energy-Density Physics: Fundamentals, Inertial Fusion, and Experimental Astrophysics*, Shock Wave and High Pressure Phenomena (Springer, 2006).
- [4] S. Basu and H. M. Antia, *Physics Reports* **457**, 217 (2008).
- [5] A. M. Serenelli, *Astrophys Space Sci* **328**, 13 (2009).
- [6] J. E. Bailey, G. A. Rochau, R. C. Mancini, C. A. Iglesias, J. J. MacFarlane, I. E. Golovkin, C. Blancard, P. Cosse, and G. Faussurier, *Physics of Plasmas* **16**, 058101 (2009).
- [7] J. E. Bailey, G. A. Rochau, C. A. Iglesias, J. J. Abdallah, J. J. MacFarlane, I. Golovkin, P. Wang, R. C. Mancini, P. W. Lake, T. C. Moore, M. Bump, O. Garcia, and S. Mazevet, *Physical Review Letters* **99**, 265002 (2007).
- [8] T. Nagayama, J. E. Bailey, G. Loisel, S. B. Hansen, G. A. Rochau, R. C. Mancini, J. J. MacFarlane, and I. Golovkin, *Physics of Plasmas* **21**, 056502 (2014).
- [9] J. E. Bailey, T. Nagayama, G. P. Loisel, G. A. Rochau, C. Blancard, J. Colgan, P. Cosse, G. Faussurier, C. J. Fontes, F. Gilleron, I. Golovkin, S. B. Hansen, C. A. Iglesias, D. P. Kilcrease, J. J. MacFarlane, R. C. Mancini, S. N. Nahar, C. Orban, J. C. Pain, A. K. Pradhan, M. Sherrill, and B. G. Wilson, *Nature* **517**, 56 (2015).
- [10] S. J. Davidson, J. M. Foster, C. C. Smith, K. A. Warburton, and S. J. Rose, *Appl. Phys. Lett.* **52**, 847 (1988).
- [11] J. Foster, D. Hoarty, C. Smith, P. Rosen, S. Davidson, S. Rose, T. Perry, and F. Serduke, *Physical Review Letters* **67**, 3255 (1991).
- [12] T. Perry, S. Davidson, F. Serduke, D. Bach, C. Smith, J. Foster, R. Doyas, R. Ward, C. Iglesias, F. Rogers, J. Abdallah, R. Stewart, J. Kilkenny, and R. Lee, *Physical Review Letters* **67**, 3784 (1991).
- [13] P. Springer, D. Fields, B. Wilson, J. Nash, W. Goldstein,

- C. Iglesias, F. Rogers, J. Swenson, M. Chen, A. Bar-Shalom, and R. Stewart, *Physical Review Letters* **69**, 3735 (1992).
- [14] L. Da Silva, B. MacGowan, D. Kania, B. Hammel, C. Back, E. Hsieh, R. Doyas, C. Iglesias, F. Rogers, and R. Lee, *Physical Review Letters* **69**, 438 (1992).
- [15] G. Winhart, K. Eidmann, C. A. Iglesias, A. Bar-Shalom, E. Mínguez, A. Rickert, and S. J. Rose, *Journal of Quantitative Spectroscopy and Radiative Transfer* **54**, 437 (1995).
- [16] P. T. Springer, K. L. Wong, C. A. Iglesias, J. H. Hammer, J. L. Porter, A. Toor, W. H. Goldstein, B. G. Wilson, F. J. Rogers, C. Deeney, D. S. Dearborn, C. Bruns, J. Emig, and R. E. Stewart, *Journal of Quantitative Spectroscopy and Radiative Transfer* **58**, 927 (1997).
- [17] C. Chenais Popovics, H. Merdji, T. Missalla, F. Gilleron, J. C. Gauthier, T. Blenski, F. Perrot, M. Klapisch, C. Bauche-Arnoult, J. Bauche, A. Bachelier, and K. Eidmann, *ApJS* **127**, 275 (2000).
- [18] C. Chenais-Popovics, M. Fajardo, F. Gilleron, U. Teubner, J. C. Gauthier, C. Bauche-Arnoult, A. Bachelier, J. Bauche, T. Blenski, F. Thais, F. Perrot, A. Benuzzi, S. Turck-Chieze, J. P. Chièze, F. Dorchie, U. Andiel, W. Foelsner, and K. Eidmann, *Phys. Rev. E* **65**, 016413 (2001).
- [19] J. E. Bailey, P. Arnault, T. Blenski, G. Dejonghe, O. Peyrusse, J. J. MacFarlane, R. C. Mancini, M. E. Cuneo, D. S. Nielsen, and G. A. Rochau, *Journal of Quantitative Spectroscopy and Radiative Transfer* **81**, 31 (2003).
- [20] P. Renaudin, C. Blancard, J. Bruneau, G. Faussurier, J. E. Fuchs, and S. Gary, *Journal of Quantitative Spectroscopy and Radiative Transfer* **99**, 511 (2006).
- [21] G. A. Rochau, J. E. Bailey, R. E. Falcon, G. P. Loisel, T. Nagayama, R. C. Mancini, I. Hall, D. E. Winget, M. H. Montgomery, and D. A. Liedahl, *Physics of Plasmas* **21**, 056308 (2014).
- [22] S. A. Slutz, K. J. Peterson, R. A. Vesey, R. W. Lemke, J. E. Bailey, W. Varnum, C. L. Ruiz, G. W. Cooper, G. A. Chandler, G. A. Rochau, and T. A. Mehlhorn, *Physics of Plasmas* **13**, 102701 (2006).
- [23] D. H. McDaniel, M. G. Mazarakis, D. E. Bliss, J. M. Elizondo, H. C. Harjes, H. C. Ives, D. L. Kitterman, J. E. Maenchen, T. D. Pointon, S. E. Rosenthal, D. L. Smith, K. W. Struve, W. A. Stygar, E. A. Weinbrecht, D. L. Johnson, and J. P. Corley, *Dense Z-Pinches* **651**, 23 (2002).
- [24] T. J. Nash, G. A. Rochau, and J. E. Bailey, *Rev. Sci. Instrum.* **81**, 10E518 (2010).
- [25] T. J. Nash, M. S. Derzon, G. A. Chandler, D. L. Fehl, R. J. Leeper, J. L. Porter, R. B. Spielman, C. Ruiz, G. Cooper, J. McGurn, M. Hurst, D. Jobe, J. Torres, J. Seaman, K. Struve, S. Lazier, T. Gilliland, L. A. Ruggles, W. A. Simpson, R. Adams, J. A. Seaman, D. Wenger, D. Nielsen, P. Riley, R. French, B. Stygar, T. Wagoner, T. W. L. Sanford, R. Mock, J. Asay, C. Hall, M. Knudson, J. Armijo, J. McKenney, R. Hawn, D. Schroen-Carey, D. Hebron, T. Cutler, S. Dropinski, C. Deeney, P. D. LePell, C. A. Coverdale, M. Douglas, M. Cuneo, D. Hanson, J. E. Bailey, P. Lake, A. Carlson, C. Wakefield, J. Mills, J. Slopek, T. Dinwoodie, and G. Idzorek, *Rev. Sci. Instrum.* **72**, 1167 (2001).
- [26] J. E. Bailey, G. A. Rochau, R. C. Mancini, C. A. Iglesias, J. J. MacFarlane, I. E. Golovkin, J. C. Pain, F. Gilleron, C. Blancard, P. Cosse, G. Faussurier, G. A. Chandler, T. J. Nash, D. S. Nielsen, and P. W. Lake, *Rev. Sci. Instrum.* **79**, 113104 (2008).
- [27] J. J. MacFarlane, *Journal of Quantitative Spectroscopy and Radiative Transfer* **81**, 287 (2003).
- [28] T. Nagayama, J. E. Bailey, G. Loisel, G. A. Rochau, and R. E. Falcon, *Rev. Sci. Instrum.* **85**, 11D603 (2014).
- [29] J. MacFarlane, I. Golovkin, R. Mancini, L. Welser, J. Bailey, J. Koch, T. Mehlhorn, G. Rochau, P. Wang, and P. Woodruff, *Phys. Rev. E* **72**, 066403 (2005).
- [30] J. J. MacFarlane, I. E. Golovkin, and P. R. Woodruff, *Journal of Quantitative Spectroscopy and Radiative Transfer* **99**, 381 (2006).
- [31] J. J. MacFarlane, I. E. Golovkin, P. R. Woodruff, and D. R. Welch, in *International Symposium on Inertial Fusion Science and Applications 2003* (2003) p. 457.
- [32] M. E. Sherill, private communication.
- [33] G. Loisel, J. E. Bailey, G. A. Rochau, G. S. Dunham, L. B. Nielsen-Weber, and C. R. Ball, *Rev. Sci. Instrum.* **83**, 10E133 (2012).